Nano Energy 89 (2021) 106373

Contents lists available at ScienceDirect

Nano Energy

journal homepage: www.elsevier.com/locate/nanoen

# Utilizing the unique charge extraction properties of antimony tin oxide nanoparticles for efficient and stable organic photovoltaics

Chao Liu [a,b], Roberto Félix [c], Karen Forberich [a,d], Xiaoyan Du [a,d], Thomas Heumüller [a,d], Gebhard J. Matt [a], Ening Gu [a], Jonas Wortmann [a], Yicheng Zhao [a], Yuanyuan Cao [e], Yakun He [a,b], Lei Ying [f], Alina Hauser [g], Marek F. Oszajca [g], Benjamin Hartmeier [g], Michael Rossier [g], Norman A. Lüchinger [g], Yi-Sheng Liu [h], Jinghua Guo [h], Kaiqi Nie [c], Regan G. Wilks [c,i], Julien Bachmann [e,j], Marcus Bär [c,i,k,l], Ning Li [a,d,m,*], Christoph J. Brabec [a,d,*]

[a] Institute of Materials for Electronics and Energy Technology (i-MEET), Department of Materials Science and Engineering, Friedrich-Alexander University Erlangen-Nürnberg, 91058 Erlangen, Germany
[b] Erlangen Graduate School in Advanced Optical Technologies (SAOT), Paul-Gordan-Straße 6, 91052 Erlangen, Germany
[c] Department Interface Design, Helmholtz-Zentrum Berlin für Materialien und Energie GmbH, Albert-Einstein-Str. 15, 12489 Berlin, Germany
[d] Helmholtz-Institute Erlangen-Nürnberg for Renewable Energy (HI ERN), Immerwahrstr. 2, 91058 Erlangen, Germany
[e] Chemistry of Thin Film Materials, Department of Chemistry and Pharmacy, Friedrich-Alexander University Erlangen-Nürnberg, IZNF, Cauerstr. 3, 91058 Erlangen, Germany
[f] Institute of Polymer Optoelectronic Materials and Devices, State Key Laboratory of Luminescent Materials and Devices, South China University of Technology, Guangzhou 510640, China
[g] Avantama Ltd., Stafa, Laubisrutistr. 50, Zurich CH-8712, Switzerland
[h] Advanced Light Source (ALS), Lawrence Berkeley National Laboratory, 1 Cyclotron Rd, Berkeley, CA 94720, USA
[i] Energy Materials In-situ Laboratory Berlin (EMIL), Helmholtz-Zentrum Berlin für Materialien und Energie GmbH, Albert-Einstein-Str. 15, 12489 Berlin, Germany
[j] Saint-Petersburg State University, Institute of Chemistry, Universitetskii pr. 26, 198504 Saint Petersburg, Russia
[k] Department of Chemistry and Pharmacy, Friedrich-Alexander-Universität Erlangen-Nürnberg, Egerlandstr. 3, 91058 Erlangen, Germany
[l] Helmholtz-Institute Erlangen-Nürnberg for Renewable Energy (HI ERN), Albert-Einstein-Str. 15, 12489 Berlin, Germany
[m] National Engineering Research Center for Advanced Polymer Processing Technology, Zhengzhou University, Zhengzhou 450002, China

ARTICLE INFO

*Keywords:*
Organic photovoltaics
Antimony doped tin oxide
Interface engineering
Doping mechanism
Metal oxide nanoparticles

ABSTRACT

Simultaneously enhancing device performance and longevity, as well as balancing the requirements on cost, scalability, and simplification of processing, is the goal of interface engineering of organic solar cells (OSCs). In our work, we strategically introduce antimony ($Sb^{3+}$) cations into an efficient and generic n-type $SnO_2$ nanoparticles (NPs) host during the scalable flame spray pyrolysis synthesis. Accordingly, a significant switch of conduction property from an n-type character to a p-type character is observed, with a corresponding shift in the work function (WF) from 4.01 ± 0.02 eV for pristine $SnO_2$ NPs to 5.28 ± 0.02 eV for $SnO_2$ NPs with 20 mol. % Sb content (ATO). Both pristine $SnO_2$ and ATO NPs with fine-tuned optoelectronic properties exhibit remarkable charge carrier extraction properties, excellent UV resistance and photo-stability being compatible with various state-of-the-art OSCs systems. The reliable and scalable pristine $SnO_2$ and ATO NPs processed by doctor-blading in air demand no complex post-treatment. Our work offers a simple but unique approach to accelerate the development of advanced interfacial materials, which could circumvent the major existing interfacial problems in solution-processed OSCs.

## 1. Introduction

Massive endeavors have been devoted to developing the power conversion efficiency (PCE) of organic solar cells (OSCs) with the certified efficiency values surpassing 18% [1] such as the development of advanced photovoltaic semiconductors [2–4], understanding and

* Corresponding authors at: Institute of Materials for Electronics and Energy Technology (i-MEET), Department of Materials Science and Engineering, Friedrich-Alexander University Erlangen-Nürnberg, 91058 Erlangen, Germany.
*E-mail addresses:* ning.li@fau.de (N. Li), christoph.brabec@fau.de (C.J. Brabec).

https://doi.org/10.1016/j.nanoen.2021.106373
Received 17 April 2021; Received in revised form 22 June 2021; Accepted 23 July 2021
Available online 27 July 2021

optimization of microstructural morphology [5–7], interfacial engineering, etc [8–10]. A typical OSC architecture comprises a bulk-heterojunction (BHJ) active layer sandwiched between two charge-collecting electrodes; as such, interfacial engineering is a decisive processing step for maximizing PCEs and device lifetime by lowering the interface energy barrier, suppressing interfacial recombination losses, and transporting charges to respective electrodes, thus enhancing charge-collection efficiency in such a stratified configuration [9,11]. At present, various approaches have been successfully employed to engineer interfacial properties via manipulating interfacial surface states, energy level offsets or work function (WF) of interfacial materials, aiming at efficient charge carrier collection and prolonged device lifetime. For instance, some studies modified the electrode with ultra-thin surface dipole layers ($\leq$ 10 nm) such as functional self-assembled monolayers (SAMs) [12–14] or polymeric electrolytes [15–17] to induce an energy-level shift, and produce a more favorable energetic alignment at the interfaces; some reports described the introduction of an interfacial layer (typically $\geq$ 10 nm) with appropriate WF as a cascading energy-level interlayer using materials such as metal oxides [18,19], metal salts/complexes [20,21], doped organic or inorganic interface materials [8, 22–25], or inorganic-organic hybrids/bilayers [26–30].

While various kinds of interfacial materials have been reported for OSCs, universal and reliable interface materials are still absent. Such generic interface materials are urgently required to simultaneously meet the requirements on cost, scalability, and plain processing, as well as efficiency and longevity, even if changing the semiconductor generation. Among abundantly available charge transporting materials (CTMs), transition metal oxides (TMOs) are promising interfacial materials owing to their attractive merits such as tunable electronic properties, high transparency in the visible range, stable chemical structure in ambient environment, etc [8,31]. However, the most commonly used solution-processed TMO ETMs such as zinc oxide (ZnO) and titanium oxide ($TiO_x$) are controversially reported as they can cause a severe photocatalytic reaction with the photoactive layer; [32] "photo-induced" shunts, originating from their intrinsic ultraviolet response, which would be detrimental to device stability are one frequently reported instability mechanism [33]. Solution-processed TMOs like molybdenum oxides ($MoO_3$) and vanadium pentoxide ($V_2O_5$) are widely investigated HTMs supposed to replace the "gold standard" poly(3, 4-ethylenedioxythiophene):poly(styrenesulfonate) (PEDOT:PSS), which induces interfacial instability between the selective active layer components and electrodes materials [34,35]. The majority reported solution-processing TMOs still require additional post-treatment such as high annealing temperature (250 °C) [36], $O_2$-plasma treatment [37], or hydrolysis [38,39], for full functionality. Such harsh post-treatment conditions are raising concerns for large-area manufacturing.

Recently, tin oxide ($SnO_2$) has attracted great attention as an efficient and stable ETM for perovskite solar cells due to its high transmittance in the whole visible wavelength range, excellent chemical stability, high UV-resistance property, stable WF, and low photocatalytic activity, etc [40]. $SnO_2$ shows its promising potential to tackle some of the issues mentioned above for OSCs as well. Nevertheless, only limited investigations about the application of $SnO_2$ as an efficient interlayer in OSCs have been reported [32, 41–43]. Moreover, $SnO_2$ nanoparticles (NPs) were reported to be intrinsically n-type, generally limiting them to ETM application, i.e., they are not suited to address issues at the p-type interface.

To adequately exploit the potential of $SnO_2$ interfacial materials, we demonstrate in this work a simple but elegant concept to develop an advanced novel HTM based on the efficient and versatile $SnO_2$ NPs. Inspired by the classic semiconductor doping mechanisms, extrinsic dopants provide extra electrons or holes to a crystalline host lattice depending on the valence state of the doping element, leading to a change in conductivity type and a shift of the Fermi level ($E_F$) inside the band gap [44,45]. Specifically, we find that the $SnO_2$:Sb (ATO) NPs show almost textbook semiconductor behaviors with respect to their bulk ensemble properties. The electronic properties change from an n-type to a p-type semiconductor with a corresponding WF shift from $4.01 \pm 0.02$ for pristine $SnO_2$ NPs to $5.28 \pm 0.02$ eV for ATO NPs with 20 mol. % Sb. At the same time, a conductivity enhancement by approximately three orders of magnitude is observed. These results suggest that the addition of Sb atoms into the flame pyrolysis synthesis of $SnO_2$ NPs indeed results in the p-type doping (presumable by $Sb^{3+}$ derived states) of the $SnO_2$ crystal lattices. Overall, ATO NPs can exhibit promising optoelectronic properties for serving as an efficient HTM. We perform a side by side comparison between PEDOT:PSS and ATO NPs for various OSCs and systematically investigate the properties of this novel material system. Importantly, reliable and scalable pristine $SnO_2$ and ATO NPs are processed by blade-coating without any complex post-treatment, demonstrating their potential to fulfill all specifications required for a low-cost, large-scale and high-throughput production process for organic photovoltaics.

## 2. Results and discussion

### 2.1. OSCs-based on pristine $SnO_2$ ETM

N-type $SnO_2$ NPs were prepared by flame spray pyrolysis synthesis, a synthesis method which can be easily scaled from lab to fab. The schematic diagram is shown in Fig. S1. OSCs were fabricated in the inverted configuration with a layer sequence of indium tin oxide (ITO)/electron transporting material (ETM)/photoactive layer/$MoO_3$/Ag, as shown in Fig. 1A. To verify the functionality of blade-coated $SnO_2$ NPs in comparison with the conventionally used ZnO ETM, we first employed a highly stable and reproducible photoactive layer based on diketopyrrolopyrrolethiophene alternating copolymer (pDPP5T-2) and [6,6]-phenyl $C_{60}$-butyric acid methyl ester ([60]PCBM). Device performance in dependence of the thickness of $SnO_2$ films was first investigated, showing that device with a thickness of ~25 nm produces optimal device performance (Fig. S2 and Table S2); devices with thicker $SnO_2$ films exhibit lower performance mainly due to increased series resistance ($R_s$). In addition, device combining as-prepared $SnO_2$ ETM exhibits comparable performance to that with $SnO_2$ ETM treated at 80 °C for 5 min in ambient (Fig. S3 and Table S3). Hence, as-prepared $SnO_2$ ETM with an optimal thickness of ~25 nm is used for further characterization. The transmittance spectra of ZnO (~30 nm) and $SnO_2$ (~25 nm) films in Fig. 1B show high transparency in the whole wavelength range; it is worth noting that there is an obvious UV-absorption band in the ZnO sample, which is absent in the $SnO_2$ sample due to its larger optical band gap energy ($E_{opt}$) (Fig. S4).

Fig. 1C shows the photocurrent density-voltage (*J-V*) characteristics of inverted OSCs incorporating ZnO or $SnO_2$ as an ETM measured under simulated AM 1.5G irradiation (100 mW $cm^{-2}$). The photovoltaic parameters, including PCE, open-circuit voltage ($V_{OC}$), short-circuit current density ($J_{SC}$), and fill factor (*FF*) are summarized in Table 1. In line with the literature [46], the device with an as-cast $SnO_2$ film delivered a PCE of 5.51%, a $V_{OC}$ of 0.57 V, a $J_{SC}$ of $-$ 14.63 mA $cm^{-2}$, and an *FF* of 65.6%, which is comparable to that of the control device based on ZnO, achieving a PCE of 5.47%, along with a $V_{OC}$ of 0.57 V, a $J_{SC}$ of $-$ 14.71 mA $cm^{-2}$, and an *FF* of 63.7%. The $J_{SC}$ values estimated from the external quantum efficiency (EQE) are in good agreement with the measured $J_{SC}$ values (Fig. S5). However, ZnO-based devices required UV light soaking from simulated AM 1.5G solar spectrum (100 mW $cm^{-2}$) to reduce the $R_s$; as a negative side effect, the leakage current-induced shunt resistance ($R_{sh}$) was decreased upon a 20 min UV exposure (Fig. 1D), while the $SnO_2$-based OSCs were rather stable under the same condition (Fig. 1E) [47]. Further in-depth investigations were conducted with a series of state-of-the-art organic photovoltaic semiconductors, including PCE-10:[70]PCBM, PCE-10:IEICO-4F, PCE-10:O-IDTBR, and PM6: Y6:[70]PCBM. The chemical structures of these organic semiconductors are listed in Fig. S6 and the corresponding energy levels

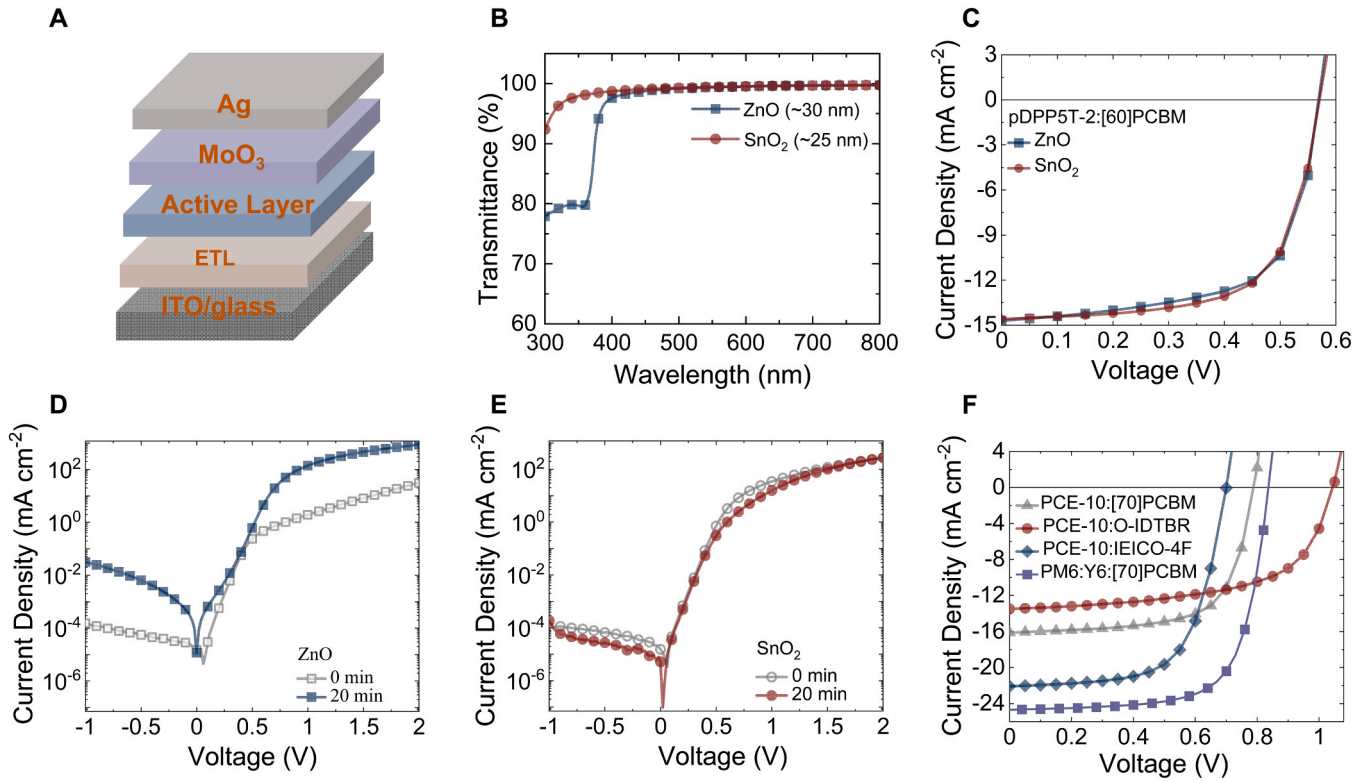


**Fig. 1.** (A) The inverted device structure used to assess the functionality of $SnO_2$ NPs; (B) transmittance spectra of ZnO and $SnO_2$ films coated on glass substrates; (C) *J-V* curves of the devices based on a pDPP5T-2:[60]PCBM active layer under AM 1.5G illumination; the evolution of *J-V* dark characteristics of devices based a pDPP5T-2:[60]PCBM active layer with (D) ZnO and (E) $SnO_2$ under AM 1.5G illumination; (F) *J-V* curves of devices with $SnO_2$ ETM based on PCE-10:[70]PCBM, PCE-10:O-IDTBR, PCE-10:IEICO-4F and PM6:Y6:[70]PCBM active layers, respectively under AM 1.5G illumination.

**Table 1**
PV performance of inverted OSCs based on different active layers with ZnO or $SnO_2$ as ETM.

| Active layer | ETM | $J_{SC}$ (mA $cm^{-2}$) | $V_{OC}$ (V) | FF (%) | PCE (%) |
|---|---|---|---|---|---|
| pDPP5T-2:[60]PCBM | ZnO | -14.71 ± 0.35 (−14.34)[a] | 0.57 ± 0.01 | 63.7 ± 1.8 | 5.47 ± 0.63 |
| pDPP5T-2:[60]PCBM | $SnO_2$ | -14.63 ± 0.27 (−14.62)[a] | 0.57 ± 0.01 | 65.60 ± 1.3 | 5.51 ± 0.35 |
| PCE-10:[70]PCBM | $SnO_2$ | -16.12 ± 0.46 (−16.08)[a] | 0.79 ± 0.01 | 67.1 ± 2.2 | 8.56 ± 0.11 |
| PCE-10:O-IDTBR | $SnO_2$ | -13.49 ± 0.57 (−13.10)[a] | 1.04 ± 0.005 | 59.7 ± 0.8 | 8.42 ± 0.03 |
| PCE-10:IEICO-4F | $SnO_2$ | -22.08 ± 0.37 (−21.15)[a] | 0.70 ± 0.002 | 64.51 ± 1.8 | 9.98 ± 0.11 |
| PM6:Y6:[70]PCBM | $SnO_2$ | -24.69 ± 0.42 (24.25)[a] | 0.84 ± 0.003 | 69.9 ± 0.3 | 14.23 ± 0.38 |

[a] Estimated from EQE spectra. Data present the average values of 12 devices.

alignments of $SnO_2$ together with those of different active layers are illustrated in Fig. S7. As summarized in Fig. 1F and Table 1, the performance of OSCs based on $SnO_2$ NPs is comparable to the values reported in the literature for OSCs based on optimized ZnO [48,49]. The corresponding EQE spectra of optimized OSCs incorporating the $SnO_2$ ETM are depicted in Fig. S8. Under continuous 1-sun illumination provided by white LED, OSCs based on $SnO_2$ NPs exhibited comparable device stability to that based on optimized ZnO NPs (Fig. S9).

### 2.2. Characterization of ATO NPs

So far, we noticed the absence of light soaking and photo-shunt as potential advantages of n-type $SnO_2$ NPs over ZnO based ETMs. Next, we extended our investigations to the ATO NPs and clarified the nature of the polarity and the doping mechanism. We selected $Sb^{3+}$ for two reasons: firstly, $Sb^{3+}$ is expected to be a p-type dopant as compared to $Sb^{5+}$; second, $Sb^{3+}$ (0.76 Å) has an ion radius which is comparable to that of $Sn^{4+}$ (0.69 Å) [50], potentially facilitating substitutional doping rather than interstitial doping. Nevertheless, the nature of the doping mechanisms is usually more complex in oxides and especially in metal oxide NPs. The schematic diagram of the proposed doping mechanism is illustrated in Fig. 2A, i.e., the $Sn^{4+}$ sites in the host matrices are supposed to be partially substituted by the lower valence $Sb^{3+}$ cations, inducing shallow acceptor levels close to the valence band. The Sb dopants introduced during spray pyrolysis are easily ionized [51–53]. Even in the case of oxide formation, $Sb_2O_3$ and $Sb_2O_5$, antimony would retain either the $Sb^{3+}$ or $Sb^{5+}$ state by sharing their 5s and 5p electrons. In the first case, one $Sb^{3+}$ cation could generate an additional shallow energy state in the $SnO_2$ lattice; hence, the successful substitutional doping process can be described by the following equation,

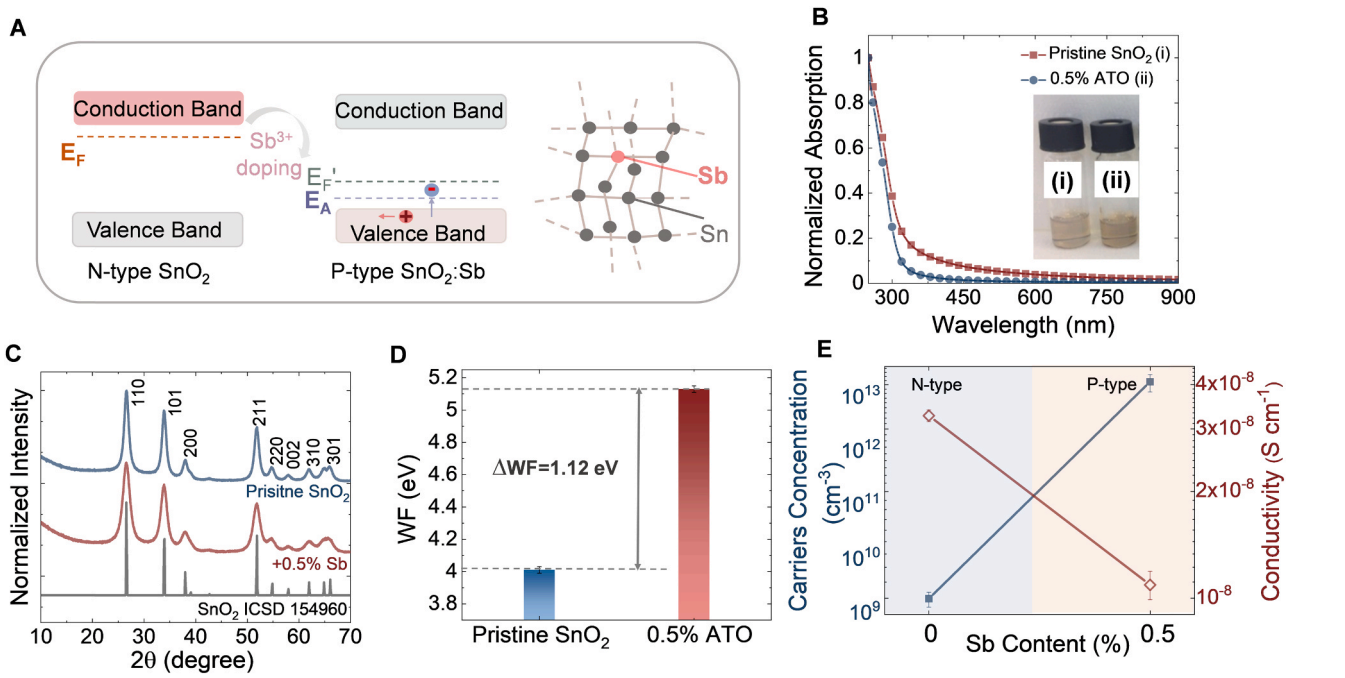


**Fig. 2.** (A) Schematic of the proposed doping mechanism: incorporation $Sb^{3+}$ into the $SnO_2$ lattice. $E_A$ denotes the shallow acceptor energy levels which are created by the $Sb^{3+}$ atoms. These energy levels can accept electrons from the valence band, thus creating holes as the mobile majority charge carriers in the valence band; (B) normalized UV–vis absorption spectra of pristine $SnO_2$ film and 0.5% ATO NPs thin film deposited onto a glass substrate; the inserted image shows dispersions of the two NPs in mixed butanol used to prepare the thin films; (C) XRD patterns, (D) WFs, and (E) charge carrier concentrations as well as conductivities of pristine $SnO_2$ and 0.5% ATO NPs.

$$Sn^{4+}\uparrow \rightarrow Sb^{3+}\downarrow + V^{-} + h^{+}, \quad (1)$$

where the symbols ↑ and ↓ denote the replacement of $Sn^{4+}$ cation by $Sb^{3+}$ cation in the lattice sites; $V^{-}$ is the shallow acceptor level; $h^{+}$ is the positively charged "free hole carrier".

To validate the feasibility of our concept, we first used a low Sb content (0.5 mol%) to dope $SnO_2$ NPs during the synthesis of NPs. As depicted in Fig. 2B, the absorption edge of 0.5% ATO film shows a reduced absorption in the visible region compared to that of the pristine $SnO_2$ film. X-ray powder diffraction (XRD) measurements were performed to characterize and compare the formation of pristine $SnO_2$ and 0.5% ATO NPs. As described in Fig. 2C, the main diffraction peaks of 0.5% ATO NPs, oriented along the (110), (101), (200), and (211), are all well assigned to tetragonal rutile $SnO_2$ (ICSD card: 154960), indicating the same rutile lattice structure [54]. No additional peaks were detected, suggesting the absence of other crystalline phases such as tin (II) oxide or antimony oxides [55,56]. Nevertheless, upon the addition of the Sb dopant, a prominent broadening of the XRD peaks could be detected, as shown in Fig. S10, suggesting a smaller crystalline domain size and/or the distortion of the local lattice matrices due to the successful incorporation of Sb atoms into the $SnO_2$ lattices [57–59]. As depicted in Fig. 2D and Table S1, by loading 0.5% Sb content, the WF of doped $SnO_2$ NPs is significantly increased from 4.01 ± 0.02 eV for pristine $SnO_2$ to 5.13 ± 0.02 eV, which reflects a remarkable change in charge carrier type in 0.5% ATO compared to the host $SnO_2$ material [60,61]. Electrical properties are shown in Fig. 2E, that the pristine $SnO_2$ film exhibits a relatively low conductivity of $3.27 \times 10^{-8}$ S $cm^{-1}$ and an electron concentration of $1.76 \times 10^{9}$ $cm^{-3}$, indicating its intrinsic n-type character due to oxygen vacancies and/or tin interstitials vacancies [62,63]. Hall effect measurements were conducted to study charge carrier concentrations of pristine $SnO_2$ and 0.5% ATO NPs. Notably, by adding 0.5% Sb dopant, Hall effect measurements evidence that the dominant charge carriers in doped $SnO_2$ film are holes with a concentration of $1.83 \times 10^{13}$ $cm^{-3}$, demonstrating a solid p-type character. The conductivity of 0.5% ATO NPs ($1.08 \times 10^{-8}$ S $cm^{-1}$) is slightly decreased due to the reduced hole mobility as shown in Fig. S11.

Since doping concentration could play a crucial role in tuning electronic structures and properties of the host material, we further explored the effect of doping concentration on the properties of the ATO NPs by extending the Sb concentration to a wider range (specifically, 2%, 5%, 10%, 20%, 30%, and 50%, denoting the nominal concentrations for the preparation of ATO NPs, instead of the effective doping concentrations). Fig. 3A exhibits the XRD patterns of doped $SnO_2$ NPs with different Sb concentrations, which confirm that all Sb-doped samples continue to agree with the tetragonal rutile structure of $SnO_2$ NPs without the presence of new crystalline peaks, even up to 50% Sb content. We acknowledge that not all Sb cations can be incorporated into the $SnO_2$ lattice at such high Sb doping concentrations. Nevertheless, XRD did not detect any new crystalline phases at such high-doping concentrations, most likely due to the formation of amorphous oxide phases, supported by x-ray absorption spectroscopy measurement (XAS) (further discussed in Fig. S12) [59]. Likewise, by analyzing the overlapped XRD patterns of all doped samples (Fig. S13A), no distinct shifts of XRD peaks are observed; however, an increased broadening of the peaks was detected, which indicates the enlarged local lattice distortion due to the increased Sb concentrations – an effect which is as well corroborated by XAS results (Fig. S12) [58]. Estimated from the most intense peak (110) with the Scherrer equation [64], the crystallite size (Dc) gradually decreases from ~ 7.66 nm of pristine $SnO_2$ NPs to ~ 4.18 nm of 50% Sb-doped NPs (Fig. S13B and Table S1). In line with the reported work, an intense bluish coloration was observed in the doped $SnO_2$ solutions with the increased Sb content loading (Fig. S14A), which possibly indicates the coexistence of the mixture of antimony valence states ($Sb^{3+}$ and $Sb^{5+}$) in the doped $SnO_2$ lattices [59,65]. In addition, the detected $E_{opt}$ values of the ATO NPs were found to increase from 4.07 eV to 4.29 eV with increasing the Sb doping concentration from 0.5% to 50% (Fig. S14B, C and Table S1). The influence of Sb concentration was further investigated by measuring the variations of the WF and conductivity, as summarized in Fig. 3B and Table S1. When the Sb doping level increased, the conductivity initially increased to the optimal value of over $3 \times 10^{-5}$

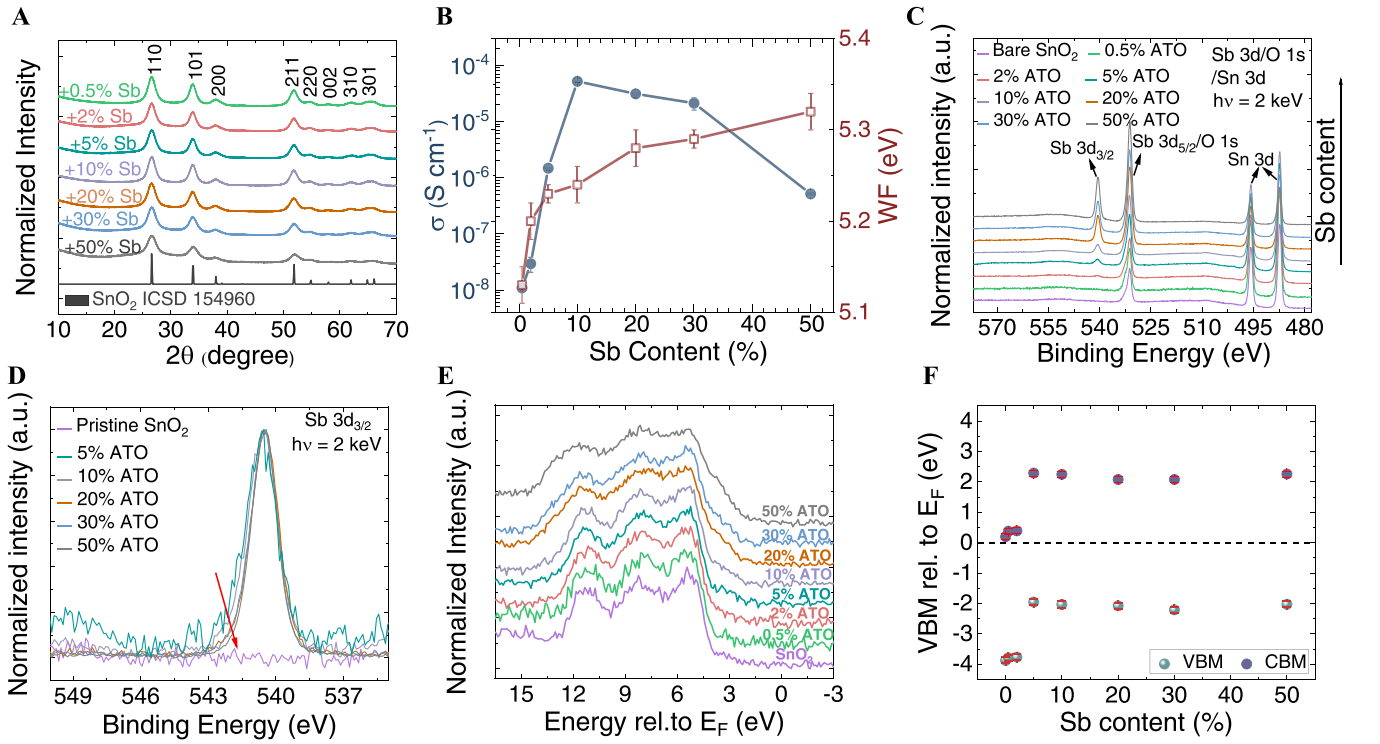


**Fig. 3.** (A) XRD patterns, (B) the variations of the conductivity (blue) and WF (wine) of ATO NPs as a function of Sb doping content (pristine $SnO_2$ is not included); (C) HAXPES spectra of the Sn 3d, Sb 3d, and O1s core level region of the investigated sample series, which were normalized to background intensity; (D) HAXPES spectra focusing on the Sb $3d_{3/2}$ line, normalized to maximum intensity (except for the pristine $SnO_2$, 0.5% and 2% ATO samples). (E) HAXPES spectra in the vicinity of the VB of the investigated sample series; (F) VBM and CBM of ATO NPs as a function of Sb content. The VBM values were determined by linear extrapolation of the leading edge of the HAXPES spectra in the vicinity of the VB from (E); and the CBM values were calculated as follows: CBM = VBM + $E_{opt}$, using the optical $E_{opt}$ values of the samples (see SI, Fig. S17 and Table S1). No clear change in VBM position were presented for samples with 0.5% and 2% Sb, which should be attributed to the similar energy position of the Sn 5s and Sb 5s states.

S $cm^{-1}$ at 10–20% Sb content, which is approximately three orders of magnitude higher than that of pristine $SnO_2$ owing to the sharp increase in hole concentration (Fig. S15); however, a deterioration of electrical conductivity is observed at higher Sb doping concentration, ascribed to the further intensified degradation of the crystalline structure and a concomitant decrease in the hole concentration [66,67]. Meanwhile, a gradual increase in WF from 5.13 ± 0.02 eV for 2% Sb content to 5.32 ± 0.02 eV for 50% Sb content was observed, opening an optimization route to deliberately tune the energy level alignment with a wide range of organic photovoltaic materials. A gradually increasing hole concentration pushes the $E_F$ to a deeper position in the ATO gap, leading to a higher WF value. Nevertheless, in a higher doping concentration, a gradual increase in WF still was observed with a decrease of the hole concentration, probably mainly due to the less-conductive surface of ATO NPs.

Our electronic measurements uniquely evidence $SnO_2$ NPs as non-stoichiometrically n-type doped, which becomes compensationally p-type doped upon addition of antimony. Having established a macroscopic model allowing to understand the properties of $SnO_2$ upon doping with antimony, we wanted to elucidate the interplay of $Sb^{3+}$ and $Sb^{5+}$ ions and their relevance for doping. Hard X-ray photoelectron spectroscopy (HAXPES) measurements were conducted with 2 keV excitation energy to analyze the chemical structure of $SnO_2$ and ATO NPs. The survey spectra of the sample series, along with photoemission line identification, are found in Fig. S16. Fig. 3C presents the spectra of the ATO series in the Sn 3d and the overlapping Sb 3d/O1s peaks regions. The Sn doublets are centered at binding energies (BEs) of ~ 487.6 ± 0.1 eV for $3d_{5/2}$ and ~ 495.9 ± 0.1 eV for $3d_{3/2}$, in agreement with literature values for $SnO_2$ [68], while the BE of the Sb doublets are centered at ~ 531.2 ± 0.1 eV for $3d_{5/2}$ and ~ 540.50 ± 0.1 eV for $3d_{3/2}$. With increasing the nominal Sb doping concentration, an increase in the Sb-related signal and a decrease in Sn-related signal are observed, trends expected for a scenario in which the $Sn^{4+}$ ions are substituted by Sb cations in the $SnO_2$ lattice matrices. In Fig. S17D, the Sn 3d peaks are slightly broadened towards higher BE with increasing Sb content; this effect could have different plausible origins such as different screening effects in the HAXPES measurements [69–72], changes in energy loss features related to changes in electronic structure, or due to the presence of an increasing amount of amorphous oxide (discussed above). The aforementioned intense bluish coloration of the solution (Fig. S14A) indicates the possibility of coexistence of two different antimony oxidation states $Sb^{3+}$ and $Sb^{5+}$, which is inevitable in this doping case. Hence, Sb 3d core levels (specifically the Sb $3d_{3/2}$ line, as there is a superposition of the Sb $3d_{5/2}$ and the O 1s line) were closely analyzed. As shown in Fig. 3D, the Sb $3d_{3/2}$ peak profile tends to narrow as a function of Sb content, suggesting the presence of the mixed Sb chemical environment in samples with low Sb doping. The curve fit analysis (shown in Fig. S17B) reveals the presence of at least two contributions. The principal and secondary contribution are found at a BE of ~540.5 eV and at a higher BE of 541.4 eV, respectively. Based on the BE values of the HAXPES Sb $3d_{3/2}$ spectra and the HAXPES-derived surface composition of the sample series, we ascribe the principal Sb $3d_{3/2}$ component to be due to a mixed $Sb^{3+}/Sb^{5+}$ valency (see Figs. S17 and S18 in SI for further discussion). By combining the results from the Hall effect measurement that all ATO samples present solid hole conduction properties (Fig. 2E, Fig. S15, and Table S1), it is thus reasonable to conclude that the $Sb^{3+}$ type cations are the predominant dopant in the ATO NPs.

The influence of different doping concentrations on the position of the valence band maximum (VBM) with respect to Fermi level ($E_F$) was further investigated by HAXPES with 2 keV excitation energy. Fig. 3E and F show full HAXPES valence band (VB) spectra and the VBM positions of the pristine $SnO_2$ NPs and ATO NPs, respectively (the details on

VBM determination are shown in Fig. S19 and Table S1). Note that we ascribe the derived VBM position to represent the near-surface electronic structure of the pristine $SnO_2$ NPs and ATO NPs. ATO NPs series maintain similar spectral shape with that of pristine $SnO_2$, which display a characteristic three-peaked structure [73,74]. For the pristine $SnO_2$ NPs, linear extrapolation of the main edge gives a VBM position of (3.87 ± 0.10) eV with respect to $E_F$. The proximity of the measured VBM and $E_{opt}$ values (i.e., 4.07 eV; see SI, Fig. S14C) for this pristine $SnO_2$ sample place the $E_F$ very close to the conduction band minimum (CBM), in agreement with the (above discussed) n-type character of the $SnO_2$ NPs on the sample surface. Additional intensity centered at ~3 eV was attributed to $Sn^{2+}$-derived Sn 5s states (see discussion in conjunction with Fig. S19 for more details) [69,72,75]. With the introduction of Sb, the VBM of the samples shift closer to $E_F$ mainly due to the emergence of Sb 5s states. Because of the similar energy position of the Sn 5s and Sb 5s states, no clear change in VBM position is apparent for samples with low Sb content (i.e., 0.5% and 2%). In samples with higher Sb content, the Sb 5s density of state (DOS) becomes a more distinctive feature, even turning into the dominant leading edge for the most Sb-rich samples (e.g., 50% Sb doping). As determined by linear extrapolation of the leading edge of HAXPES VB spectra, the VBM position shifts from 3.87 ± 0.10 eV relative to $E_F$ for the pristine $SnO_2$ NPs to (2.03 ± 0.10) eV for the 50% Sb sample. These results highlight the pronounced change in doping character exhibited by the sample series: starting with pristine $SnO_2$ NPs with a pronounced n-type doping character (indicated by $E_F$ being close to the CBM) and $E_F$ shifting closer to the VBM for (the surface of) Sb-rich samples (i.e. a p-type doping character), in agreement with the conduction type change evidenced by Hall effect measurement. Another interesting question in the n- or p-type doping of nanocrystals is the energetic position of the dopant, which is typically discussed in terms of impurity doping. Assuming that the addition of 0.5–50% Sb could be fully doped into $SnO_2$ lattices, nevertheless, Hall effect measurements identify an increase in the hole carrier concentration only from about $10^{13}$ to $10^{16}$ $cm^{-3}$ upon doping, which suggests that at most ppm levels of the added Sb atoms are actively ionized and contribute to the conduction process; most of the Sb dopants likely form deep energy levels or/and are compensated and have no contribution to the free carrier concentration. Additionally, we want to point out that the absorption measurements (Fig. S14) reveal a shift of the optical $E_{opt}$ and even more conclusive, a stark change in oscillator strength in the

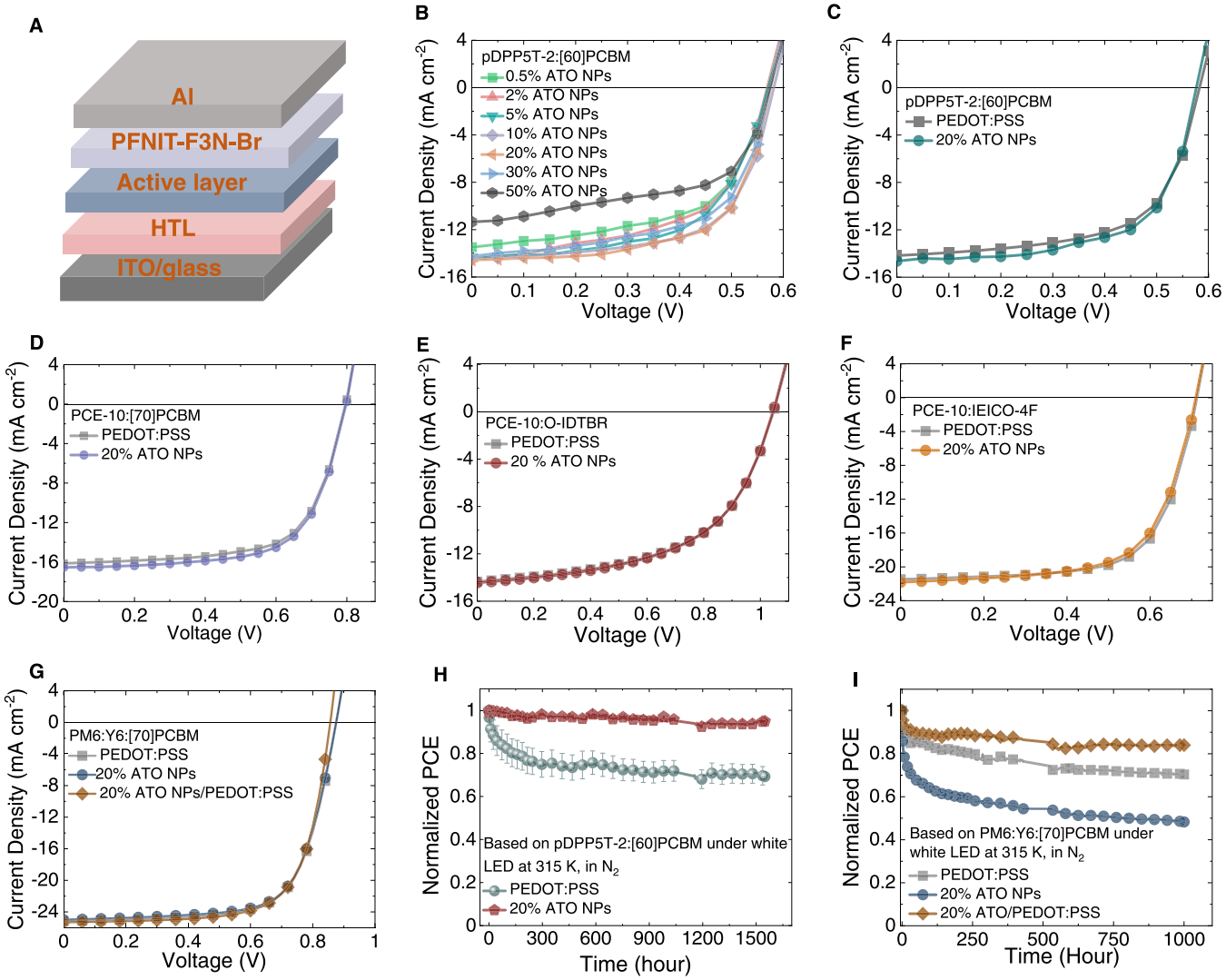


**Fig. 4.** (A) Device structure used to assess the functionality of ATO NPs; (B) *J-V* characteristics of devices based on pDPP5T-2:[60]PCBM incorporating different ATO HTMs under AM 1.5G illumination condition; illuminated *J-V* characteristics of devices based on (C) pDPP5T-2:[60]PCBM, (D) PCE-10:[70]PCBM, (E) PCE-10:O-IDTBR, (F) PCE-10:IEICO-4F, and (G) PM6:Y6:[70]PCBM with PEDOT:PSS or 20% ATO NPs film as HTM. *J-V* characteristics of devices based on PM6:Y6:[70]PCBM with combined 20% ATO NPs/PEDOT:PSS HTMs was also present in (G); (H) the photo-stability tests of pDPP5T-2:[60]PCBM-based OSCs in a regular device architecture based on PEDOT:PSS or 20% ATO NPs as HTM; (I) the photo-stability tests of PM6:Y6:[70]PCBM-based OSCs in a regular device architecture based on PEDOT:PSS or 20% ATO NPs or 20% ATO NPs/PEDOT:PSS bilayer as HTM; For combined interlayers, PEDOT:PSS was deposited on top of 20% ATO NPs.

sub-bandgap regime. Lacking further evidence, we propose that energetically broad impurity doping is a likely mechanism to explain the behavior of excess antimony in ATO NPs.

### 2.3. OSCs-based on ATO NPs HTM

In order to verify the potential of various ATO NPs as HTMs in OSCs, we first fabricated pDPP5T-2:[60]PCBM-based OSCs in a regular device architecture, as shown in Fig. 4A. All the ATO HTMs were doctor-bladed without any post-treatment during device fabrication. Fig. S20 presents the transmittance spectra of all ATO layers with high transparency of over 90% in the 300–800 nm region. The *J-V* characteristics of OSCs under AM 1.5G radiation spectra are presented in Fig. 4B, and the corresponding PV parameters are summarized in Table 2. It is observed that the performance of OSCs was gradually improved as the Sb doping concentration increased. The optimal device performance was achieved for ATO NPs with a 10–20% doping level based on pDPP5T-2:[60]PCBM. At higher Sb loading, device performance decreases mainly because of $J_{SC}$ and *FF* losses, which we ascribe to the lowered charge transporting property and enhanced charge recombination; in addition, rough surface morphology also likely affects the charge extraction at the ATO HTL/active layer interface in the case. The EQE spectra of the corresponding OSCs are depicted in Fig. S21. We also provide counter-evidence for the charge selectivity of ATO NPs. OSCs in an inverted device architecture incorporating ATO as ETMs showed a negligible PV response, demonstrating excellent unipolar hole extraction performance. At doping level larger than 2% the device starts to behave as a photoconductor with negligible rectification of ATO NP layers (Fig. S22 and Table S4).

Based on the above exploration, 20% ATO NPs were selected for further device investigations. It was found that for pDPP5T-2:[60]PCBM-based OSCs the 20% ATO films with a thickness of ~40 nm deliver optimal device performance (Fig. S23 and Table S5); further increasing the layer thickness led to reduced device performance mainly due to increased series resistance. Furthermore, it is most encouraging that 20% ATO HTM based OSCs showed full *J-V* performance without UV activation as documented by the absence of light soaking and remain stable under continuous AM 1.5G illumination (100 mW $cm^{-2}$) for up to 20 min (Fig. S24 and Table S6). Finally, OSCs fabricated using doped $SnO_2$ NPs (20% Sb) as HTM and pristine $SnO_2$ NPs as ETM exhibited comparable performance to that of control devices, highlighting the excellent optoelectronic properties of $SnO_2$ and ATO NPs as charge transporting layers (CTMs) in OSCs (Fig. S25 and Table S7).

The compatibility of 20% ATO HTM with various photoactive materials was further investigated in the regular device structure. The corresponding energy alignment diagram is plotted in Fig. S26, showing its favorable energetic alignment with respect to the applied organic semiconductors. As presented in Fig. 4C–G and Fig. S27B–E (full device parameters are summarized in Table 3), all OSCs with 20% ATO NPs delivered comparable state-of-the-art PV efficiencies to that using the well-known PEDOT:PSS, demonstrating its great versatility.

Understanding and eliminating the stability limitation imposed by the interface layers, for instance, the acidic and hygroscopic nature of the most commonly used PEDOT:PSS, is essential for solution-processed OSCs. The long-term stability of OSCs based on 20% ATO NPs or PEDOT:PSS was investigated with various organic semiconductors under identical operational conditions. In order to eliminate the influence of the photoactive layer on the stability study, we first investigated the stability of ATO-based OSCs using pDPP5T-2:[60]PCBM, which was found to be one of the most stable organic semiconductor blends for solar cell applications [76,77]. As depicted in Fig. 4H, the long-term performance of regular architecture pDPP5T-2:[60]PCBM-based OSCs using PEDOT:PSS and PFNIT-F3N-Br solution processed interfaces was overall stable but showed a distinct “burn-in” degradation, retaining 78% of the initial PCE after over 1500 h of continuous one sun illumination. Burn-in degradation is frequently associated with a change in microstructure; [78] however, it can be also related to interface degradation between ITO electrode and PEDOT:PSS, which is most prominently seen as an *FF* loss (Fig. S28) [34–35, 79]. Encouragingly, pDPP5T-2:[60]PCBM-based OSCs with 20% ATO NPs as HTM exhibited clearly improved photo-stability with negligible performance loss under the same measurement conditions. However, we found that this observation cannot be directly transferred to any other materials system. Contrarily, we found initially reduced device stability, for the material system PM6:Y6:[70]PCBM. As shown in Fig. 4I and Fig. S29, the device longevity of PM6:Y6:[70]PCBM-based OSCs using PEDOT:PSS maintained 69% of their initial PCE after 1000 h of continuous one sun illumination, which is mainly due to FF degradation. Surprisingly, PM6:Y6:[70]PCBM-based devices with a 20% ATO HTM exhibited a massive $V_{OC}$ burn-in degradation,

**Table 2**
PV performance of pDPP5T-2:[60]PCBM-based devices with different ATO NPs as HTMs in the regular structure.

| HTM | $J_{SC}$ (mA $cm^{-2}$) | $V_{OC}$ (V) | FF (%) | PCE (%) |
|---|---|---|---|---|
| 0.5% ATO NPs | -13.56 ± 0.26 (13.25)[a] | 0.56 ± 0.01 | 58.3 ± 1.2 | 4.42 ± 0.32 |
| 2% ATO NPs | -14.29 ± 0.14 (−14.13)[a] | 0.57 ± 0.01 | 56.3 ± 1.3 | 4.61 ± 0.18 |
| 5% ATO NPs | -14.39 ± 0.19 (−14.34)[a] | 0.57 ± 0.01 | 59.7 ± 2.2 | 4.90 ± 0.43 |
| 10% ATO NPs | -14.48 ± 0.14 (−14.23)[a] | 0.58 ± 0.01 | 62.7 ± 2.1 | 5.33 ± 0.31 |
| 20% ATO NPs | -14.65 ± 0.21 (−14.19)[a] | 0.58 ± 0.01 | 63.5 ± 2.1 | 5.41 ± 0.45 |
| 30% ATO NPs | -14.27 ± 0.29 (−13.83)[a] | 0.56 ± 0.01 | 60.6 ± 0.8 | 4.85 ± 0.25 |
| 50% ATO NPs | -10.79 ± 0.34 (−10.49)[a] | 0.58 ± 0.01 | 56.1 ± 0.9 | 3.55 ± 0.34 |

[a] Estimated from EQE spectra. Data present the average values of 12 devices.

**Table 3**
PV performance of devices using PEDOT:PSS or 20% ATO NPs film as HTM with different photoactive layers in the regular structure.

| HTM | $J_{SC}$ (mA $cm^{-2}$) | $V_{OC}$ (V) | FF (%) | PCE (%) |
|---|---|---|---|---|
| pDPP5T-2:[60]PCBM | | | | |
| PEDOT:PSS | -14.18 ± 0.11 (−14.15)[a] | 0.58 ± 0.01 | 62.1 ± 1.3 | 5.16 ± 0.58 |
| 20% ATO NPs | -14.65 ± 0.21 (14.19)[a] | 0.58 ± 0.01 | 63.5 ± 2.1 | 5.41 ± 0.64 |
| PCE-10:[70]PCBM | | | | |
| PEDOT:PSS | -16.13 ± 0.46 (−15.63)[a] | 0.80 ± 0.01 | 66.5 ± 2.5 | 8.56 ± 0.13 |
| 20% ATO NPs | -16.52 ± 0.39 (−15.89)[a] | 0.80 ± 0.01 | 66.5 ± 1.8 | 8.78 ± 0.25 |
| PCE-10:O-IDTBR | | | | |
| PEDOT:PSS | -14.36 ± 0.13 (−13.78)[a] | 1.04 ± 0.005 | 54.5 ± 2.5 | 8.21 ± 0.33 |
| 20% ATO NPs | -14.46 ± 0.19 (−13.69)[a] | 1.04 ± 0.005 | 54.4 ± 3.0 | 8.23 ± 0.54 |
| PCE-10:IEICO-4F | | | | |
| PEDOT:PSS | -22.46 ± 0.55 (−21.98)[a] | 0.71 ± 0.01 | 65.4 ± 1.7 | 10.37 ± 0.36 |
| 20% ATO NPs | -21.84 ± 0.46 (−21.64)[a] | 0.71 ± 0.01 | 65.0 ± 1.2 | 10.11 ± 0.26 |
| | | PM6:Y6:[70]PCBM | | |
| PEDOT:PSS | -25.21 ± 0.33 (24.37)[a] | 0.87 ± 0.002 | 68.94 ± 0.17 | 15.15 ± 0.22 |
| 20% ATO NPs | -25.02 ± 0.68 (24.41)[a] | 0.87 ± 0.002 | 69.28 ± 0.31 | 15.17 ± 0.41 |
| 20% ATO NPs/ PEDOT:PSS | -25.35 ± 0.61 (24.50)[a] | 0.86 ± 0.003 | 70.21 ± 0.44 | 15.31 ± 0.59 |

[a] Estimated from EQE spectra. Data present the average values of 12 devices.

leading to a sharp drop in PCE within the first 100 h, accompanied by minor FF losses. We screened the stability of various ATO-based OSCs and found that the burn-in degradation in $V_{OC}$ is semiconductor-dependent (Fig. S30). While pDPP5T-2:[60]PCBM-based OSCs as well as P3HT:o-IDTBR harmonized with ATO NPs film, PM6-based and PCE-10-based devices suffer from rapid $V_{OC}$ burn-in losses. We mimicked different loss mechanisms by drift diffusion simulation, trying to rationalize bulk recombination from work function shifts and interface induced (trap assisted) recombination [80]. From the shape of the degradation pattern and the associated FF, as well as $J_{SC}$ losses, we exclude bimolecular bulk recombination as relevant degradation mechanism. Simulation suggests the formation of interface traps as the most likely loss mechanism for the type of ATO used in the study (see discussion in conjunction with Fig. S31 for more details). A change in the work function is currently disregarded as ATO layers do not exhibit work function variation upon light illumination (Fig. S31D). Detailed investigations on the ATO interface stability with various photoactive layers are being carried out, which are beyond the scope of the current work.

We demonstrated that PEDOT:PSS and ATO can give equally high time zero performance but both are prone to distinct degradation mechanisms. PEDOT:PSS is likely to react with the ITO electrode leading to FF burn-in losses while ATO based HTMs are likely to react with the semiconductor layer leading to a $V_{OC}$ burn-in loss during long-term stability testing. We thus decided to engineer a HTM system where each material can play its respective strengths. A bilayer of ATO and PEDOT:PSS is the most obvious option to prevent the sensitive interface reaction. We found the combination of both HTMs is a feasible and universal solution to demonstrate OSCs with high efficiency and promising stability (Fig. 4G and Table 3) if ATO is processed on top of ITO and beneath PEDOT:PSS, so that ATO is separated from semiconductor and PEDOT:PSS is separated from ITO. As shown in Fig. 4I, the interface induced device degradation (mainly *FF* losses in the case of PEDOT:PSS and $V_{OC}$ losses in the case of ATO NPs) are successfully alleviated by using the bilayer concept. Compared to the OSCs based on either PEDOT:PSS or ATO, OSCs incorporating the bilayer HTMs exhibited comparably high time-zero PCE and maintained to 84% of the initial PCE under continuous illumination for over 1000 h (Fig. 4I). These solar cells exhibit a flat performance trend after about 300–500 h, highlighting that light induced interface degradation can be indeed brought under control by sophisticated interface engineering-even for such sensitive compositions like ternary PM6:Y6:[70]PCBM blends.

## 3. Conclusion

We demonstrate an efficient and versatile $SnO_2$ NP ETM with high UV-resistance produced by flame spray pyrolysis synthesis, which circumvents the formation of "photo-induced" shunts and photocatalytic reaction issues with the photoactive layer in inverted OSCs. We successfully switched the doping character of $SnO_2$ NPs from being n-type to p-type by incorporating $Sb^{3+}$ cations during the synthesis of $SnO_2$ NPs, resulting in ATO ($SnO_2$:Sb) NPs with tunable optoelectronic properties. By combining experimental results from Hall Effect measurements and HAXPES measurements, we are able to provide profound evidence that $Sb^{3+}$ cations are the main substitutions for partial $Sn^{4+}$ sites in the $SnO_2$ lattice, leading to excess holes. OSCs based on 20% ATO NPs exhibited comparable performance to the well-known PEDOT:PSS based on various photoactive layers in normal architecture OSCs. While both interface material exhibit comparable time-zero performance, a distinctly different degradation behavior under long-time illumination is observed for the respective interface materials. More important, these interface specific device instabilities were successfully eliminated by inserting ATO between ITO and PEDOT:PSS. This bilayer stabilizes on the one hand the ITO interface and on the other hand the semiconductor interface and results in comparable time-zero performance and superior light-soaking stability for material composites, which have been discussed as inherently instable. Our work proposes a simple and viable approach for developing highly-efficient, reliable, and scalable interfacial materials based on $SnO_2$ NPs. We believe that $SnO_2$ and ATP NPs can address many of the current major interfacial challenges found for solution-processed OSCs based on high performing NFA blends. We further demonstrate that each new generation of interface material imperatively needs to be investigated with respect to time-zero performance as well as long time function stability. In this light, $SnO_2$ and derived ATO NPs are indeed an interesting and promising material concept which deserves the attention of the emerging photovoltaics community.

## CRediT authorship contribution statement

**N.L. and C.L.**: Conceptualization. **C.L., K.F., Y.Y.C., X.Y.D., J.W., T.H., G.J.M., E.G., K.N., R.G.W., M.B., Y.-S.L. and J.G.R.F.**: Investigation. **C.L., N.L. and C.J.B.**: Writing – original draft. **C.L., R.F., K.F., G.J.M., E.G., Y.C.Z., Y.Y.C., Y.K.H., K.N., R.G.W., J.B., M.B., N.L., C. J.B.**: Writing – review & editing. **L.Y., A.H., M.F.O., B.H., M.R., N.A.L.**: Resources. **N.L. and C.J.B.**: Supervision. **C.J.B.**: Funding acquisition.

## Declaration of Competing Interest

The authors declare no conflict of interest.

## Acknowledgement

C.L., Y.H. and E.G. are grateful to the financial support from China Scholarship Council (CSC) and the Erlangen Graduate School in Advanced Optical Technologies (SAOT) at FAU Erlangen-Nürnberg. K.F. gratefully acknowledges the financial support of the State of Bavaria via the project PV-Tera (No. 446521a/20/5) and of the BMWi via the project COSIMA (FKZ: 032429A). C.J.B. gratefully acknowledges the financial support through the "Aufbruch Bayern" initiative of the state of Bavaria (EnCN and "Solar Factory of the Future"), the Bavarian Initiative "Solar Technologies go Hybrid" (SolTech), and the DFG SFB 953 (Project No. 182849149), DFG INST 90/917-1 and DFG INST 90/726-3. Further support was provided by the European Research Council with a Consolidator Grant ('Solacylin', grant agreement 647281). We thank HZB for the allocation of synchrotron radiation beamtime and gratefully acknowledge the resources provided by the Advanced Light Source, a U. S. DOE Office of Science User Facility under contract no. DE-AC02-05CH11231.

## Appendix A. Supporting information

Supplementary data associated with this article can be found in the online version at doi:10.1016/j.nanoen.2021.106373.

## References

[1] Q. Liu, Y. Jiang, K. Jin, J. Qin, J. Xu, W. Li, J. Xiong, J. Liu, Z. Xiao, K. Sun, S. Yang, X. Zhang, L. Ding, 18% Efficiency organic solar cells, Sci. Bull. 65 (2020) 272–275, https://doi.org/10.1016/j.scib.2020.01.001.
[2] P. Cheng, G. Li, X. Zhan, Y. Yang, Next-generation organic photovoltaics based on non-fullerene acceptors, Nat. Photonics 12 (2018) 131–142, https://doi.org/10.1038/s41566-018-0104-9.
[3] J. Zhang, H.S. Tan, X. Guo, A. Facchetti, H. Yan, Material insights and challenges for non-fullerene organic solar cells based on small molecular acceptors, Nat. Energy 3 (2018) 720–731, https://doi.org/10.1038/s41560-018-0181-5.
[4] A. Karki, A.J. Gillett, R.H. Friend, T.Q. Nguyen, The path to 20% power conversion efficiencies in nonfullerene acceptor organic solar cells, Adv. Energy Mater. (2020), 2003441, https://doi.org/10.1002/aenm.202003441.
[5] X. Jiao, L. Ye, H. Ade, Quantitative morphology-performance correlations in organic solar cells: insights from soft X-ray scattering, Adv. Energy Mater. 7 (2017), 1700084, https://doi.org/10.1002/aenm.201700084.
[6] K. Gao, Y. Kan, X. Chen, F. Liu, B. Kan, L. Nian, X. Wan, Y. Chen, X. Peng, T. P. Russell, Y. Cao, A.K. Jen, Low-bandgap porphyrins for highly efficient organic solar cells: materials, morphology, and applications, Adv. Mater. 32 (2020), 1906129, https://doi.org/10.1002/adma.201906129.

[7] F. Liu, Y. Gu, J.W. Jung, W.H. Jo, T.P. Russell, On the morphology of polymer-based photovoltaics, J. Polym. Sci. Part B Polym. Phys. 50 (2012) 1018–1044, https://doi.org/10.1002/polb.23063.

[8] Z. Huang, D. Ouyang, C.J. Shih, B. Yang, W.C.H. Choy, Solution-processed ternary oxides as carrier transport/injection layers in optoelectronics, Adv. Energy Mater. (2019), 1900903, https://doi.org/10.1002/aenm.201900903.

[9] C.-C. Chueh, C.-Z. Li, A.K.Y. Jen, Recent progress and perspective in solution-processed Interfacial materials for efficient and stable polymer and organometal perovskite solar cells, Energy Environ. Sci. 8 (2015) 1160–1189, https://doi.org/10.1039/C4EE03824J.

[10] Z. Yin, J. Wei, Q. Zheng, Interfacial materials for organic solar cells: recent advances and perspectives, Adv. Sci. 3 (2016), 1500362, https://doi.org/10.1002/advs.201500362.

[11] H. Zhang, R.C. Shallcross, N. Li, T. Stubhan, Y. Hou, W. Chen, T. Ameri, M. Turbiez, N.R. Armstrong, C.J. Brabec, Overcoming electrode-induced losses in organic solar cells by tailoring a quasi-ohmic contact to fullerenes via solution-processed alkali hydroxide layers, Adv. Energy Mater. 6 (2016), 1502195, https://doi.org/10.1002/aenm.201502195.

[12] L. Huang, L. Chen, P. Huang, F. Wu, L. Tan, S. Xiao, W. Zhong, L. Sun, Y. Chen, Triple dipole effect from self-assembled small-molecules for high performance organic photovoltaics, Adv. Mater. 28 (2016) 4852–4860, https://doi.org/10.1002/adma.201600197.

[13] H. Choi, H.B. Kim, S.J. Ko, J.Y. Kim, A.J. Heeger, An organic surface modifier to produce a high work function transparent electrode for high performance polymer solar cells, Adv. Mater. 27 (2015) 892–896, https://doi.org/10.1002/adma.201404172.

[14] J. Min, Y.N. Luponosov, Z.-G. Zhang, S.A. Ponomarenko, T. Ameri, Y. Li, C. J. Brabec, Interface design to improve the performance and stability of solution-processed small-molecule conventional solar cells, Adv. Energy Mater. 4 (2014), 1400816, https://doi.org/10.1002/aenm.201400816.

[15] Y. Zhou, C. Fuentes-Hernandez, J. Shim, J. Meyer, A.J. Giordano, H. Li, P. Winget, T. Papadopoulos, H. Cheun, J. Kim, M. Fenoll, A. Dindar, W. Haske, E. Najafabadi, T.M. Khan, H. Sojoudi, S. Barlow, S. Graham, J.-L. Brédas, S.R. Marder, A. Kahn, B. Kippelen, A universal method to produce low–work function electrodes for organic electronics, Science 336 (2012) 327–332, https://doi.org/10.1126/science.1218829.

[16] Z. He, C. Zhong, S. Su, M. Xu, H. Wu, Y. Cao, Enhanced power-conversion efficiency in polymer solar cells using an inverted device structure, Nat. Photonics 6 (2012) 591–595, https://doi.org/10.1038/nphoton.2012.190.

[17] Y. Ge, L. Hu, L. Zhang, Q. Fu, G. Xu, Z. Xing, L. Huang, W. Zhou, Y. Chen, Polyolefin elastomer as the anode interfacial layer for improved mechanical and air stabilities in nonfullerene solar cells, ACS Appl. Mater. Interface 12 (2020) 10706–10716, https://doi.org/10.1021/acsami.9b18095.

[18] D. Ouyang, Z. Huang, W.C.H. Choy, Solution-processed metal oxide nanocrystals as carrier transport layers in organic and perovskite solar cells, Adv. Funct. Mater. 29 (2019), 1804660, https://doi.org/10.1002/adfm.201804660.

[19] S. Kim, M.A. Saeed, S.H. Kim, J.W. Shim, Enhanced hole selecting behavior of WO3 interlayers for efficient indoor organic photovoltaics with high fill-factor, Appl. Surf. Sci. 527 (2020), 146840, https://doi.org/10.1016/j.apsusc.2020.146840.

[20] Y. Jia, L. Yang, W. Qin, S. Yin, F. Zhang, J. Wei, Efficient polymer bulk heterojunction solar cells with cesium acetate as the cathode interfacial layer, Renew. Energy 50 (2013) 565–569, https://doi.org/10.1016/j.renene.2012.07.012.

[21] F. Chen, Q. Chen, L. Mao, Y. Wang, X. Huang, W. Lu, B. Wang, L. Chen, Tuning indium tin oxide work function with solution-processed alkali carbonate interfacial layers for high-efficiency inverted organic photovoltaic cells, Nanotechnology 24 (2013), 484011, https://doi.org/10.1088/0957-4484/24/48/484011.

[22] X. Lin, B. Wegner, K.M. Lee, M.A. Fusella, F. Zhang, K. Moudgil, B.P. Rand, S. Barlow, S.R. Marder, N. Koch, A. Kahn, Beating the thermodynamic limit with photo-activation of n-doping in organic semiconductors, Nat. Mater. 16 (2017) 1209–1215, https://doi.org/10.1038/nmat5027.

[23] S. Guo, S.B. Kim, S.K. Mohapatra, Y. Qi, T. Sajoto, A. Kahn, S.R. Marder, S. Barlow, n-Doping of organic electronic materials using air-stable organometallics, Adv. Mater. 24 (2012) 699–703, https://doi.org/10.1002/adma.201103238.

[24] Q. Kang, Z. Zheng, Y. Zu, Q. Liao, P. Bi, S. Zhang, Y. Yang, B. Xu, J. Hou, n-doped inorganic molecular clusters as a new type of hole transport material for efficient organic solar cells, Joule 5 (2021) 646–658, https://doi.org/10.1016/j.joule.2021.01.011.

[25] S. Biswas, Y.-J. You, J. Kim, S.R. Ha, H. Choi, S.-H. Kwon, K.-K. Kim, J.W. Shim, H. Kim, Decent efficiency improvement of organic photovoltaic cell with low acidic hole transport material by controlling doping concentration, Appl. Surf. Sci. 512 (2020), 145700, https://doi.org/10.1016/j.apsusc.2020.145700.

[26] Z. Zheng, Q. Hu, S. Zhang, D. Zhang, J. Wang, S. Xie, R. Wang, Y. Qin, W. Li, L. Hong, N. Liang, F. Liu, Y. Zhang, Z. Wei, Z. Tang, T.P. Russell, J. Hou, H. Zhou, A highly efficient non-fullerene organic solar cell with a fill factor over 0.80 enabled by a fine-tuned hole-transporting layer, Adv. Mater. 30 (2018), 1801801, https://doi.org/10.1002/adma.201801801.

[27] J. Troughton, M. Neophytou, N. Gasparini, A. Seitkhan, F.H. Isikgor, X. Song, Y.-H. Lin, T. Liu, H. Faber, E. Yengel, J. Kosco, M.F. Oszajca, B. Hartmeier, M. Rossier, N.A. Lüchinger, L. Tsetseris, H.J. Snaith, S. De Wolf, T.D. Anthopoulos, I. McCulloch, D. Baran, A universal solution processed interfacial bilayer enabling ohmic contact in organic and hybrid optoelectronic devices, Energy Environ. Sci. 13 (2020) 268–276, https://doi.org/10.1039/C9EE02202C.

[28] H. Azimi, T. Ameri, H. Zhang, Y. Hou, C.O.R. Quiroz, J. Min, M. Hu, Z.-G. Zhang, T. Przybilla, G.J. Matt, E. Spiecker, Y. Li, C.J. Brabec, A universal interface layer based on an amine-functionalized fullerene derivative with dual functionality for efficient solution processed organic and perovskite solar cells, Adv. Energy Mater. 5 (2015), 1401692, https://doi.org/10.1002/aenm.201401692.

[29] T. Stubhan, M. Salinas, A. Ebel, F.C. Krebs, A. Hirsch, M. Halik, C.J. Brabec, Increasing the fill factor of inverted P3HT:PCBM solar cells through surface modification of Al-doped ZnO via phosphonic acid-anchored C60 SAMs, Adv. Energy Mater. 2 (2012) 532–535, https://doi.org/10.1002/aenm.201100668.

[30] C. Hou, H. Yu, Modifying the nanostructures of PEDOT:PSS/Ti3C2TX composite hole transport layers for highly efficient polymer solar cells, J. Mater. Chem. C 8 (2020) 4169–4180, https://doi.org/10.1039/D0TC00075B.

[31] J. Meyer, S. Hamwi, M. Kroger, W. Kowalsky, T. Riedl, A. Kahn, Transition metal oxides for organic electronics: energetics, device physics and applications, Adv. Mater. 24 (2012) 5408–5427, https://doi.org/10.1002/adma.201201630.

[32] Y. Jiang, L. Sun, F. Jiang, C. Xie, L. Hu, X. Dong, F. Qin, T. Liu, L. Hu, X. Jiang, Photocatalytic effect of ZnO on the stability of nonfullerene acceptors and its mitigation by $SnO_2$ for nonfullerene organic solar cells, Mater. Horiz. 6 (2019) 1438–1443, https://doi.org/10.1039/C9MH00379G.

[33] G. Kim, J. Kong, J. Kim, H. Kang, H. Back, H. Kim, K. Lee, Overcoming the light-soaking problem in inverted polymer solar cells by introducing a heavily doped titanium sub-oxide functional layer, Adv. Energy Mater. 5 (2015), 1401298, https://doi.org/10.1002/aenm.201401298.

[34] M.P. de Jong, L.J. van Ijzendoorn, M.J.A. de Voigt, Stability of the interface between indium-tin-oxide and poly(3,4-ethylenedioxythiophene)/poly (styrenesulfonate) in polymer light-emitting diodes, Appl. Phys. Lett. 77 (2000) 2255–2257, https://doi.org/10.1063/1.1315344.

[35] A. Garcia, G.C. Welch, E.L. Ratcliff, D.S. Ginley, G.C. Bazan, D.C. Olson, Improvement of interfacial contacts for new small-molecule bulk-heterojunction organic photovoltaics, Adv. Mater. 24 (2012) 5368–5373, https://doi.org/10.1002/adma.201200963.

[36] T. Yang, M. Wang, Y. Cao, F. Huang, L. Huang, J. Peng, X. Gong, S.Z.D. Cheng, Y. Cao, Polymer solar cells with a low-temperature-annealed sol-gel-derived MoOx film as a hole extraction layer, Adv. Energy Mater. 2 (2012) 523–527, https://doi.org/10.1002/aenm.201100598.

[37] J. Meyer, R. Khalandovsky, P. Gorrn, A. Kahn, MoO3 films spin-coated from a nanoparticle suspension for efficient hole-injection in organic electronics, Adv. Mater. 23 (2011) 70–73, https://doi.org/10.1002/adma.201003065.

[38] K. Zilberberg, S. Trost, H. Schmidt, T. Riedl, Solution processed vanadium pentoxide as charge extraction layer for organic solar cells, Adv. Energy Mater. 1 (2011) 377–381, https://doi.org/10.1002/aenm.201100076.

[39] K. Zilberberg, S. Trost, J. Meyer, A. Kahn, A. Behrendt, D. Lützenkirchen-Hecht, R. Frahm, T. Riedl, Inverted organic solar cells with sol-gel processed high work-function vanadium oxide hole-extraction layers, Adv. Funct. Mater. 21 (2011) 4776–4783, https://doi.org/10.1002/adfm.201101402.

[40] Q. Jiang, X. Zhang, J. You, SnO2: a wonderful electron transport layer for perovskite solar cells, Small 14 (2018), 1801154, https://doi.org/10.1002/smll.201801154.

[41] L. Zuo, Q. Chen, N. De Marco, Y.T. Hsieh, H. Chen, P. Sun, S.Y. Chang, H. Zhao, S. Dong, Y. Yang, Tailoring the interfacial chemical interaction for high-efficiency perovskite solar cells, Nano Lett. 17 (2017) 269–275, https://doi.org/10.1021/acs.nanolett.6b04015.

[42] S. Trost, K. Zilberberg, A. Behrendt, T. Riedl, Room-temperature solution processed SnOx as an electron extraction layer for inverted organic solar cells with superior thermal stability, J. Mater. Chem. 22 (2012) 16224, https://doi.org/10.1039/C2JM33445C.

[43] T. Becker, S. Trost, A. Behrendt, I. Shutsko, A. Polywka, P. Görrn, P. Reckers, C. Das, T. Mayer, D. Di Carlo Rasi, K.H. Hendriks, M.M. Wienk, R.A.J. Janssen, T. Riedl, All-oxide MoOx/SnOx charge recombination interconnects for inverted organic tandem solar cells, Adv. Energy Mater. 8 (2018), 1702533, https://doi.org/10.1002/aenm.201702533.

[44] P. Würfel, U.X. Würfel, Physics of Solar Cells: From Basic Principles to Advanced Concepts, John Wiley & Sons, 2016.

[45] J. Nelson, The Physics of Solar Cells, World Scientific Publishing Company, 2003.

[46] X. Du, O. Lytken, M.S. Killian, J. Cao, T. Stubhan, M. Turbiez, P. Schmuki, H.-P. Steinrück, L. Ding, R.H. Fink, N. Li, C.J. Brabec, Overcoming interfacial losses in solution-processed organic multi-junction solar cells, Adv. Energy Mater. 7 (2017), 1601959, https://doi.org/10.1002/aenm.201601959.

[47] S. Trost, T. Becker, A. Polywka, P. Görrn, M.F. Oszajca, N.A. Luechinger, D. Rogalla, M. Weidner, P. Reckers, T. Mayer, T. Riedl, Avoiding photoinduced shunts in organic solar cells by the use of tin oxide (SnOx) as electron extraction material instead of ZnO, Adv. Energy Mater. 6 (2016), 1600347, https://doi.org/10.1002/aenm.201600347.

[48] C. Liu, X. Du, S. Gao, A. Classen, A. Osvet, Y. He, K. Mayrhofer, N. Li, C.J. Brabec, A cross-linked interconnecting layer enabling reliable and reproducible solution-processing of organic tandem solar cells, Adv. Energy Mater. 10 (2020), 1903800, https://doi.org/10.1002/aenm.201903800.

[49] L. Perdigon-Toro, H. Zhang, A. Markina, J. Yuan, S.M. Hosseini, C.M. Wolff, G. Zuo, M. Stolterfoht, Y. Zou, F. Gao, D. Andrienko, S. Shoaee, D. Neher, Barrierless free charge generation in the high-performance PM6:Y6 bulk heterojunction non-fullerene solar cell, Adv. Mater. 32 (2020), 1906763, https://doi.org/10.1002/adma.201906763.

[50] J. Rockenberger, U. zum Felde, M. Tischer, L. Tröger, M. Haase, H. Weller, Near edge X-ray absorption fine structure measurements (XANES) and extended x-ray absorption fine structure measurements (EXAFS) of the valence state and coordination of antimony in doped nanocrystalline SnO2, J. Chem. Phys. 112 (2000) 4296–4304, https://doi.org/10.1063/1.480975.

[51] A.R. Babar, K.Y. Rajpure, Effect of intermittent time on structural, optoelectronic, luminescence properties of sprayed antimony doped tin oxide thin films, J. Anal. Appl. Pyrolysis 112 (2015) 214–220, https://doi.org/10.1016/j.jaap.2015.01.024.
[52] V. Fauzia, M.N. Yusnidar, L.H. Lalasari, A. Subhan, A.A. Umar, High figure of merit transparent conducting Sb-doped SnO 2 thin films prepared via ultrasonic spray pyrolysis, J. Alloy. Compd. 720 (2017) 79–85, https://doi.org/10.1016/j.jallcom.2017.05.243.
[53] S. Yu, W. Zhang, L. Li, D. Xu, H. Dong, Y. Jin, Fabrication of p-type SnO2 films via pulsed laser deposition method by using Sb as dopant, Appl. Surf. Sci. 286 (2013) 417–420, https://doi.org/10.1016/j.apsusc.2013.09.107.
[54] J. Ni, X. Zhao, X. Zheng, J. Zhao, B. Liu, Electrical, structural, photoluminescence and optical properties of p-type conducting, antimony-doped SnO2 thin films, Acta Mater. 57 (2009) 278–285, https://doi.org/10.1016/j.actamat.2008.09.013.
[55] H.S. Chin, K.Y. Cheong, K.A. Razak, Review on oxides of antimony nanoparticles: synthesis, properties, and applications, J. Mater. Sci. 45 (2010) 5993–6008, https://doi.org/10.1007/s10853-010-4849-x.
[56] C.M. Campo, J.E. Rodriguez, A.E. Ramirez, Thermal behaviour of romarchite phase SnO in different atmospheres: a hypothesis about the phase transformation, Heliyon 2 (2016) 00112, https://doi.org/10.1016/j.heliyon.2016.e00112.
[57] J. Ni, X. Zhao, J. Zhao, P-type transparent conducting SnO2:Zn film derived from thermal diffusion of Zn/SnO2/Zn multilayer thin films, Surf. Coat. Technol. 206 (2012) 4356–4361, https://doi.org/10.1016/j.surfcoat.2012.04.031.
[58] N. Phung, R. Felix, D. Meggiolaro, A. Al-Ashouri, E.S.G. Sousa, C. Hartmann, J. Hidalgo, H. Kobler, E. Mosconi, B. Lai, R. Gunder, M. Li, K.L. Wang, Z.K. Wang, K. Nie, E. Handick, R.G. Wilks, J.A. Marquez, B. Rech, T. Unold, J.P. Correa-Baena, S. Albrecht, F. De Angelis, M. Bar, A. Abate, The doping mechanism of halide perovskite unveiled by alkaline earth metals, J. Am. Chem. Soc. 142 (2020) 2364–2374, https://doi.org/10.1021/jacs.9b11637.
[59] Y. Nakanishi, Y. Suzuki, T. Nakamura, Y. Hatanaka, Y. Fukuda, A. Fujisawa, G. Shimaoka, Coloration of SnSbO thin films, Appl. Surf. Sci. 48 (1991) 55–58, https://doi.org/10.1016/0169-4332(91)90307-6.
[60] M. Kröger, S. Hamwi, J. Meyer, T. Riedl, W. Kowalsky, A. Kahn, P-type doping of organic wide band gap materials by transition metal oxides: a case-study on Molybdenum trioxide, Org. Electron. 10 (2009) 932–938, https://doi.org/10.1016/j.orgel.2009.05.007.
[61] V.A. Kolesov, C. Fuentes-Hernandez, W.F. Chou, N. Aizawa, F.A. Larrain, M. Wang, A. Perrotta, S. Choi, S. Graham, G.C. Bazan, T.Q. Nguyen, S.R. Marder, B. Kippelen, Solution-based electrical doping of semiconducting polymer films over a limited depth, Nat. Mater. 16 (2017) 474–480, https://doi.org/10.1038/nmat4818.
[62] Z. Jarzebski, J. Marton, Physical properties of SnO2 materials II. Electrical properties, J. Electrochem. Soc. 123 (1976) 299C–310C, https://doi.org/10.1149/1.2133090.
[63] M.-M. Bagheri-Mohagheghi, M. Shokooh-Saremi, Electrical, optical and structural properties of Li-doped SnO2transparent conducting films deposited by the spray pyrolysis technique: a carrier-type conversion study, Semicond. Sci. Technol. 19 (2004) 764–769, https://doi.org/10.1088/0268-1242/19/6/019.
[64] B. Nasr, S. Dasgupta, D. Wang, N. Mechau, R. Kruk, H. Hahn, Electrical resistivity of nanocrystalline Al-doped zinc oxide films as a function of Al content and the degree of its segregation at the grain boundaries, J. Appl. Phys. 108 (2010), 103721, https://doi.org/10.1063/1.3511346.
[65] M. Kojima, H. Kato, M. Gatto, Blackening of tin oxide thin films heavily doped with antimony, Philos. Mag. B 68 (2006) 215–222, https://doi.org/10.1080/01418639308226402.
[66] H. Zheng, L. Li, Z. Sun, S. Yu, W. Luo, Preferential orientation, microstructure and functional properties of SnO 2:Sb thin film: the effects of post-growth annealing, Appl. Surf. Sci. 362 (2016) 230–236, https://doi.org/10.1016/j.apsusc.2015.11.230.
[67] V. Müller, M. Rasp, G. Štefanić, J. Ba, S. Günther, J. Rathousky, M. Niederberger, D. Fattakhova-Rohlfing, Highly conducting nanosized monodispersed antimony-doped tin oxide particles synthesized via nonaqueous sol−gel procedure, Chem. Mater. 21 (2009) 5229–5236, https://doi.org/10.1021/cm902189r.
[68] R. Félix, N. Llobera-Vila, C. Hartmann, C. Klimm, M. Hartig, R.G. Wilks, M. Bär, Preparation and in-system study of SnCl2 precursor layers: towards vacuum-based synthesis of Pb-free perovskites, RSC Adv. 8 (2018) 67–73, https://doi.org/10.1039/C7RA12172E.
[69] F. Borgatti, J.A. Berger, D. Céolin, J.S. Zhou, J.J. Kas, M. Guzzo, C.F. McConville, F. Offi, G. Panaccione, A. Regoutz, D.J. Payne, J.-P. Rueff, O. Bierwagen, M. E. White, J.S. Speck, M. Gatti, R.G. Egdell, Revisiting the origin of satellites in core-level photoemission of transparent conducting oxides: the case of n-doped $SnO_2$, Phys. Rev. B 97 (2018), 155102, https://doi.org/10.1103/PhysRevB.97.155102.
[70] C. Körber, P. Ágoston, A. Klein, Surface and bulk properties of sputter deposited undoped and Sb-doped SnO2 thin films, Sens. Actuators B Chem. 139 (2009) 665–672, https://doi.org/10.1016/j.snb.2009.03.067.
[71] Y. Gassenbauer, R. Schafranek, A. Klein, S. Zafeiratos, M. Havecker, A. Knopgericke, R. Schlogl, Surface potential changes of semiconducting oxides monitored by high-pressure photoelectron spectroscopy: importance of electron concentration at the surface, Solid State Ion. 177 (2006) 3123–3127, https://doi.org/10.1016/j.ssi.2006.07.036.
[72] P.A. Cox, R.G. Egdell, C. Harding, W.R. Patterson, P.J. Tavener, Surface properties of antimony doped tin(IV) oxide: a study by electron spectroscopy, Surf. Sci. 123 (1982) 179–203, https://doi.org/10.1016/0039-6028(82)90322-3.
[73] M.A. Stranick, A. Moskwa, SnO2 by XPS, Surf. Sci. Spectra 2 (1993) 50–54, https://doi.org/10.1116/1.1247724.
[74] C.L. Lau, G.K. Wertheim, Oxidation of tin: an ESCA study, J. Vac. Sci. Technol. 15 (1978) 622–624, https://doi.org/10.1116/1.569642.
[75] C. Hartmann, S. Gupta, T. Bendikov, X. Kozina, T. Kunze, R. Felix, G. Hodes, R. G. Wilks, D. Cahen, M. Bar, Impact of SnF2 addition on the chemical and electronic surface structure of CsSnBr3, ACS Appl. Mater. Interface 12 (2020) 12353–12361, https://doi.org/10.1021/acsami.9b22967.
[76] S. Arumugam, D. Cortizo-Lacalle, S. Rossbauer, S. Hunter, A.L. Kanibolotsky, A. R. Inigo, P.A. Lane, T.D. Anthopoulos, P.J. Skabara, An air-stable DPP-thieno-TTF copolymer for single-material solar cell devices and field effect transistors, ACS Appl. Mater. Interface 7 (2015) 27999–28005, https://doi.org/10.1021/am5080562.
[77] L. Lucera, P. Kubis, F.W. Fecher, C. Bronnbauer, M. Turbiez, K. Forberich, T. Ameri, H.J. Egelhaaf, C.J. Brabec, Guidelines for closing the efficiency gap between hero solar cells and roll-to-roll printed modules, Energy Technol. 3 (2015) 373–384, https://doi.org/10.1002/ente.201402192.
[78] N. Li, J.D. Perea, T. Kassar, M. Richter, T. Heumueller, G.J. Matt, Y. Hou, N. S. Guldal, H. Chen, S. Chen, S. Langner, M. Berlinghof, T. Unruh, C.J. Brabec, Abnormal strong burn-in degradation of highly efficient polymer solar cells caused by spinodal donor-acceptor demixing, Nat. Commun. 8 (2017) 14541, https://doi.org/10.1038/ncomms14541.
[79] T. Heumueller, W.R. Mateker, I.T. Sachs-Quintana, K. Vandewal, J.A. Bartelt, T. M. Burke, T. Ameri, C.J. Brabec, M.D. McGehee, Reducing burn-in voltage loss in polymer solar cells by increasing the polymer crystallinity, Energy Environ. Sci. 7 (2014) 2974–2980, https://doi.org/10.1039/C4EE01842G.
[80] L.J.A. Koster, E.C.P. Smits, V.D. Mihailetchi, P.W.M. Blom, Device model for the operation of polymer/fullerene bulk heterojunction solar cells, Phys. Rev. B 72 (2005), 085205, https://doi.org/10.1103/PhysRevB.72.085205.